

Banner appropriate to article type will appear here in typeset article

# Wake Interference Effects on Flapping Dynamics of Elastic Inverted Foil

Aarshana R. Parekh<sup>1</sup> †, and Rajeev. K. Jaiman<sup>1</sup>

Mechanical Engineering Department, The University of British Columbia, Vancouver, BC, Canada V6T 1Z4

(Received xx; revised xx; accepted xx)

Using high-fidelity simulations, we study the self-induced flapping dynamics of an inverted elastic foil when it is placed in tandem with a stationary circular cylinder. The effect of wake interference on the inverted foil's coupled dynamics is systematically examined at a fixed Reynolds number ( $Re$ ) as a function of non-dimensional bending rigidity ( $K_B$ ) and the structure to fluid mass ratio ( $m^*$ ). Our results show that the inverted foil experiences a relatively higher transverse fluid loading under unsteady wake flow. Consequently, flapping instability is induced at a higher  $K_B$  value as compared to an isolated inverted elastic foil. There exists a critical  $K_{B,Cr} = 0.25$ , above which the downstream foil is synchronized with the unsteady wake, and the cylinder controls the flapping response and the wake vortex dynamics. During synchronization, two additional flapping modes are observed as a function of decreasing  $K_B$ , namely small amplitude flapping and moderate amplitude flapping modes. Below  $K_{B,Cr}$ , the downstream foil undergoes self-induced large-amplitude flapping similar to an isolated foil counterpart. Interestingly, unlike an isolated inverted foil, in the tandem setup, the flapping dynamics are strongly influenced by both  $K_B$  and  $m^*$ . The findings from this study aim to generalize our understanding of the self-induced flapping dynamics of inverted foils and have relevance to the development of inverted foil-based renewable energy harvesters.

**Key words:**

## 1. Introduction

When submerged in fluid flow, an elastic cantilevered foil experiences self-induced, self-sustained periodic oscillations, commonly known as the self-induced flapping phenomenon (Shelley and Zhang 2011). When the foil is cantilevered at the trailing edge (TE), with its leading edge (LE) left free to oscillate, i.e., the inverted configuration, its flapping response presents an intriguing fluid-structure interaction problem that is commonly observed in nature and various engineering applications. In the past few decades, the study of inverted foil flapping dynamics has observed an increase in popularity owing not only to its prevalence but also to the rich non-linear dynamics associated with complex wake vortex interactions

† Email address for correspondence: arparekh@student.ubc.ca

and large deformation of the flexible structure. Particularly, there is a need for a generalized understanding of the underlying flapping mechanism for optimization and control strategies to achieve the desired flapping response.

Studies have shown that for an inverted foil of a fixed aspect ratio ( $AR$ ) under steady uniform flow, the dynamics are characterized by three critical non-dimensional parameters, namely Reynolds number ( $Re$ ), the structure-to-fluid mass ratio ( $m^*$ ), and bending rigidity ( $K_B$ ). At a given a  $Re$ , there exists a critical  $K_{B,Cr}$  below which the inverted foil loses its stability and undergoes self-sustained flapping motion (Kim et al. 2013; Gurugubelli and Jaiman 2015; Sader et al. 2016). For a range of  $K_B$ , known as the large amplitude flapping (LAF) regime, the foil undergoes limit cycle oscillations with large peak-to-peak amplitudes. These large amplitude oscillations are driven by the combined effect of periodic vortex shedding from the leading edge and the foil's inherent fluid elastic instability (Gurugubelli and Jaiman 2019). Compared to  $K_B$ , during LAF, the dynamics are only weakly influenced by  $m^*$  and relatively insensitive to changes in  $Re$  (Gurugubelli and Jaiman 2015; Tang et al. 2015; Shoele and Mittal 2016; Gurugubelli and Jaiman 2019).

While extensive research has been conducted on inverted foil dynamics in uniform flow, recent studies have demonstrated intriguing phenomena when the foil is subject to unsteady flow, particularly the coupled dynamics of an inverted foil when placed in tandem with a rigid bluff body. Studies like (Kim et al. 2017) and (Ojo et al. 2022) have revealed that in some scenarios, due to wake interference, an additional small amplitude flapping mode is observed along with the modes observed for an isolated inverted foil. The occurrence of these different modes is determined by the balance between fluid forces arising from the foil's interaction with the unsteady wake and the structure's elastic and inertial forces. The upstream unsteady wake, in turn, is dependent on cylinder geometry and proximity.

While these findings shed light upon the inverted foil's flapping response in wake flow, its underlying physics is not completely understood and requires further investigation. Such knowledge is especially relevant in the field of small-scale renewable energy harvesting. Inverted foil has demonstrated superior energy harvesting potential. Many energy harvesting models have been proposed based on this approach wherein the fluid kinetic energy is harnessed in the form of the foil's internal strain energy during flapping and via piezoelectric material, converting it to electric power (Allen and Smits 2001; Akcabay and Young 2012; Michelin and Doaré 2013; Orrego et al. 2017). While the electric power output for these devices typically relies on the flapping amplitude and frequency of the foil, it is strongly dependent on upstream wind and ocean environments. To achieve robust energy harvesting systems with a consistent power output, it is critical to expand our knowledge of the flapping response of an inverted foil in unsteady and perturbed flow conditions, thus motivating our study toward the wake interference effect on inverted foils.

This study examines the coupled dynamics of a flexible inverted foil subject to the wake flow of an upstream rigid circular cylinder through a series of high-fidelity numerical simulations. Through a comparative study of the inverted foil response in isolated and tandem setups, we aim to investigate the following key questions: (i) How does the wake interference influence the foil's flapping response? (ii) what is the intrinsic relationship between the wake vortices and different flapping modes? and (iii) how does mass ratio influence the flapping dynamics in the tandem setup? A systematic study with the considered parameter range that addresses these questions has not yet been studied to the best of the authors' knowledge.

## 2. Problem setup and numerical methodology

We study the self-induced flapping dynamics of an inverted foil by considering a Quasi-3D computational setup. Figure 1 displays the problem setup and the computational domain with

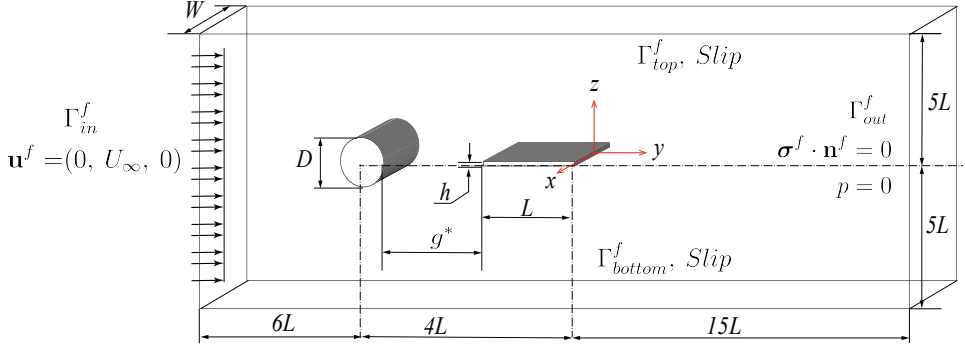


Figure 1: Schematic of the computational domain of an inverted foil placed downstream of a stationary circular cylinder

	M1	M2	M3
No. of nodes	36670	73194	149212
No. of Elements	114227	223481	451083
rms of transverse tip displacement $A_z^{rms}/L$	0.1039 (59.414%)	0.245 (4.29%)	0.256
Mean drag coefficient $\bar{C}_d$	0.0829 (70.22%)	0.2864 (2.8735%)	0.2784
rms lift coefficient $C_l^{rms}$	0.5059 (47.32%)	0.9562 (0.447%)	0.9605

Table 1: Grid convergence study results for the flexible inverted foil interacting with wake flow of a stationary circular cylinder at  $Re = 1000$ ,  $m^* = 0.1$ , and  $K_B = 0.2$

information on the boundary conditions. We consider an inverted foil  $\Omega_s$  of length  $L$ , width  $W = 0.75L$ , and thickness  $h = 0.01L$ . For the tandem arrangement, the foil is positioned in the downstream region of a rigid circular cylinder of diameter  $D$  at a streamwise distance  $g^*$  along the center line. Both setups are subjected to uniform incompressible axial flow  $\Omega_f(t)$ , with velocity magnitude  $U_\infty$  as shown in figure 1. The foil is placed with its TE at  $(0, 0, 0)$ . A uniform velocity  $\mathbf{u}^f = (0, U_\infty, 0)$  condition is applied at the inlet  $\Gamma_{in}^f$  boundary, and traction-free condition ( $\boldsymbol{\sigma}^f \cdot \mathbf{n}^f = 0$ ) is considered for the outlet  $\Gamma_{out}^f$  boundary. Here,  $\Gamma_{top}^f$  and  $\Gamma_{bottom}^f$  represent the sides of the domain where the slip condition is implemented. No-slip condition is applied for the cylinder and foil surfaces and periodic boundary condition is applied for the domain sides. The incompressible fluid flow dynamics are governed by unsteady three-dimensional Navier-Stokes equations in the arbitrary Lagrangian-Eulerian (ALE) reference frame, which are defined as:

$$\rho^f \frac{\partial \mathbf{u}^f}{\partial t} + \rho^f (\mathbf{u}^f - \mathbf{w}) \cdot \nabla \mathbf{u}^f = \nabla \cdot \boldsymbol{\sigma}^f + \mathbf{f}^f \quad \text{in } \Omega^f(t), \quad (2.1)$$

$$\nabla \cdot \mathbf{u}^f = 0 \quad \text{in } \Omega^f(t), \quad (2.2)$$

$$\boldsymbol{\sigma}^f = -p\mathbf{I} + \mathbf{T}, \quad \mathbf{T} = 2\mu^f \boldsymbol{\epsilon}^f(\mathbf{u}^f), \quad \boldsymbol{\epsilon}^f(\mathbf{u}^f) = \frac{1}{2} [\nabla \mathbf{u}^f + (\nabla \mathbf{u}^f)^T] \quad (2.3)$$

where  $\mathbf{u}^f = \mathbf{u}^f(\mathbf{x}, t)$  and  $\mathbf{w} = \mathbf{w}(\mathbf{x}, t)$  represent the fluid and mesh velocities defined at each spatial point  $\mathbf{x} \in \Omega^f(t)$ , respectively.  $\rho^f$  and  $\boldsymbol{\sigma}^f$  represent the density and Cauchy stress tensor for a Newtonian fluid as defined in equation (2.3), and  $\mathbf{f}^f$  denotes the body

force applied to the fluid.  $p$  represents the fluid pressure,  $\mathbf{I}$  denotes the second-order identity tensor, and  $\mathbf{T}$  is the viscous stress tensor.

The elastic foil's deformation is governed by the non-linear structural equation, defined as:

$$\rho^s \frac{\partial \mathbf{u}^s}{\partial t} = \nabla \cdot \boldsymbol{\sigma}^s + \mathbf{f}^s \quad \text{in } \Omega^s, \quad (2.4)$$

where  $\mathbf{u}^s = \mathbf{u}^s(\mathbf{z}, t)$  is the structural velocity defined at each point on the structure  $\mathbf{z} \in \Omega^s$ ,  $\mathbf{f}^s$  represents the fluid forces applied on the solid, and  $\boldsymbol{\sigma}^s$  denotes the first Piola-Kirchoff stress tensor. In this study, the structure is modeled as a St. Venant-Kirchoff hyperelastic material. In this coupled fluid-structure system, the velocity and traction continuity conditions are satisfied along the interface as follows:

$$\int_{\varphi^s(\gamma, t)} \boldsymbol{\sigma}^f(\boldsymbol{\varphi}^s(\mathbf{z}, t), t) \cdot \mathbf{n}^f d\Gamma + \int_{\gamma} \boldsymbol{\sigma}^s(\mathbf{z}, t) \cdot \mathbf{n}^s d\Gamma = 0 \quad \forall \gamma \subset \Gamma_0, \quad (2.5)$$

$$\mathbf{u}^f(\boldsymbol{\varphi}^s(\mathbf{z}, t), t) = \mathbf{u}^f(\mathbf{z}, t) \quad \forall \mathbf{z} \in \Gamma_0, \quad (2.6)$$

where  $\mathbf{n}^f$  and  $\mathbf{n}^s$  are the outward normals to the deformed fluid and the undeformed solid interface boundaries, respectively.  $\Gamma_0$  denotes the fluid-structure interface  $\Gamma(t)$  at time  $t = 0$ .  $\boldsymbol{\varphi}^s$  is the displacement function that maps each Lagrangian point  $\mathbf{z} \in \Omega^s$  to its deformed position at time  $t$ .  $\gamma$  is any part of the interface  $\Gamma_0$  and  $\boldsymbol{\varphi}^s(\gamma, t)$  represents the corresponding fluid part over the interface  $\Gamma(t)$  at  $t$ .

A higher-order variational method based on fully coupled three-dimensional Navier Stokes and nonlinear structural dynamic equations has been utilized to model the coupled FSI problem. This methodology is based on the combined field explicit interface (CFEI) formulation proposed by (Liu et al. 2014). The solver's numerical stability, validity, and ability to accurately simulate flapping dynamics have been demonstrated in our prior work (Liu et al. 2014; Gurugubelli and Jaiman 2015). For a detailed description of the numerical algorithm and implementation, the readers are referred to (Liu et al. 2014). To determine the adequacy of the computation mesh, a convergence study is performed for three different meshes  $M1$ ,  $M2$ , and  $M3$ . The flexible foil in the tandem arrangement has been considered at  $Re = 1000$ ,  $m^* = 0.1$ , and  $K_B = 0.2$ . Table 1 lists the r.m.s of the normalized transverse tip displacement  $A_z^{rms}/L$  and lift coefficient, as well as the mean drag coefficient for the different meshes. The bracketed values denote the percentage difference in numerical simulations with respect to mesh  $M3$ . It is seen that the relative errors using mesh  $M2$  are less than 5%; therefore, all the numerical simulations are carried out using mesh  $M2$ .

The dynamics of the flexible foil are strongly influenced by three key non-dimensional parameters, i.e.,  $Re$ ,  $K_B$  and  $m^*$ , defined as:

$$Re = \frac{\rho^f U_\infty L}{\mu^f}, \quad K_B = \frac{B}{\rho^f U_\infty^2 L^3}, \quad m^* = \frac{\rho^s h}{\rho^f L}, \quad (2.7)$$

where  $E$ ,  $\nu$ , and  $\rho^s$  denote Young's modulus, Poisson's ratio, and density, respectively.  $B$  represents the flexural rigidity, which is defined as  $B = Eh^3/12(1 - \nu^2)$ , and  $K_B$  determines the relative importance of the foil's bending force to the fluid's inertial force. The derived quantities that we study include the lift and drag force coefficients. These force coefficients are computed by integrating the element-wise contributions of pressure and viscous stresses along the foil surface. The drag coefficient  $C_d$  and lift coefficient  $C_l$  are defined as

$$C_d = \frac{1}{\frac{1}{2}\rho^f U^2 L} \int_{\Gamma} (\rho^f \cdot \mathbf{n}) \cdot \mathbf{n}_y d\Gamma, \quad C_l = \frac{1}{\frac{1}{2}\rho^f U^2 L} \int_{\Gamma} (\rho^f \cdot \mathbf{n}) \cdot \mathbf{n}_z d\Gamma, \quad (2.8)$$

where  $\mathbf{n}_y$  and  $\mathbf{n}_z$  are the Cartesian components of normal vector  $\mathbf{n}$ . Our present study considers a fixed  $g^* = 2.8L$  and  $D = 0.4L$ . The considered  $g^*$ , is greater than the critical value  $4D$  beyond which the shear layers roll up alternatively to form Kármán vortices between the cylinder and the foil only experiences wake interference effects (Zdravkovich 1987; Sharman et al. 2005).

A fixed  $Re = 1000$  and  $\nu = 0.3$  is considered, and the foil's dynamics in both isolated and tandem setups are analyzed for  $K_B \in [1 \times 10^{-3}, 1]$  and  $m^* \in [0.1, 10]$ . The non-dimensional parameters  $K_B$  and  $m^*$  are varied by changing Young's modulus and density of the structure, respectively.

### 3. Results and discussion

#### 3.1. Response characteristics

We first investigate how the flapping response changes for an inverted foil when placed in tandem with an upstream bluff body compared to the isolated case. The foil's coupled dynamics are characterized as a function of decreasing  $K_B$  at  $m^* = 0.1$ . Figure 2a shows the variation of maximum transverse tip displacements of the foil with respect to  $K_B$ . The maximum transverse tip displacement is defined as  $A_z^{max}/L = \sqrt{2}A_z^{rms}/L$ . Here  $A_z^{rms}/L$ , calculated using  $A_z^{rms}/L = \left( \sqrt{\frac{1}{n} \sum_t (A_z - \bar{A}_z)^2} \right) / L$ , where  $A_z$  and  $\bar{A}_z$  represent the transverse tip displacement and mean transverse displacement respectively. Compared to the isolated foil, for which flapping instability is observed for  $K_B < 0.35$ , in the tandem arrangement, the foil performs sustained oscillations for  $K_B \leq 1$ . Thus, the range of  $K_B$  where flapping instability is observed is wider for the inverted foil in the tandem arrangement than an isolated foil. Two additional flapping regimes are identified before the downstream foil transitions into the LAF regime based on the foil's maximum transverse tip displacement, namely the (i) small amplitude flapping regime (SAF) when  $A_z^{max}/L < 0.2$  and (ii) moderate amplitude flapping regime (MAF) when  $0.2 < A_z^{max}/L \leq 0.5$ . The typical full-body response of the downstream inverted foil in SAF, MAF, and LAF regimes is shown in figure 2a. The SAF and MAF regimes are observed for  $0.6 \leq K_B \leq 1$  and  $0.2 \leq K_B < 0.6$ , respectively. The maximum transverse tip displacement for both regimes gradually increases as  $K_B$  decreases. Consequently, the transition to LAF is smoother as compared to the isolated case. The downstream foil experiences the large amplitude flapping for a narrower range of  $K_B \in [0.1, 0.15]$  compared to the isolated case of  $K_B \in [0.1, 0.2]$ . For  $K_B < 0.1$ , as  $K_B$  is decreased, downstream foil transitions to deflected flapping mode and finally flipped flapping mode for very small  $K_B \in [0.01, 0.001]$  similar to the isolated foil.

Figure 2b shows the variation of the mean drag coefficient  $\bar{C}_d$  and the root mean square of the lift coefficient  $C_l^{rms}$  with respect to  $K_B$  for the inverted foil in both setups. Qualitatively, the drag force exerted on the inverted foil in both setups follows similar trends as a function  $K_B$ . Wherein the drag force increases as  $K_B$  decreases, instability is induced, and deformation increases. In contrast, an overall higher lift force is exerted on the downstream foil as compared to the isolated case. For  $K_B > 0.35$ , a lift coefficient for the downstream foil is around  $O(10)$  times higher than the drag force and up to  $O(10^3)$  times greater than the lift coefficient for the isolated foil thereby resulting in the early onset of flapping instability. These results demonstrate that for  $K_B > 0.35$ , the oscillations of the downstream foil in the tandem setup are driven by the fluid loading due to the unsteady wake.

Figures 2c and 2d show the power spectra of the coefficient of lift and transverse tip displacement about the mean deformed position  $(A_z - \bar{A}_z)/L$  for  $K_B \in [0.15, 0.25]$ . Here,  $f_{v,s}$  denotes the vortex shedding frequency of the upstream rigid circular cylinder. One must

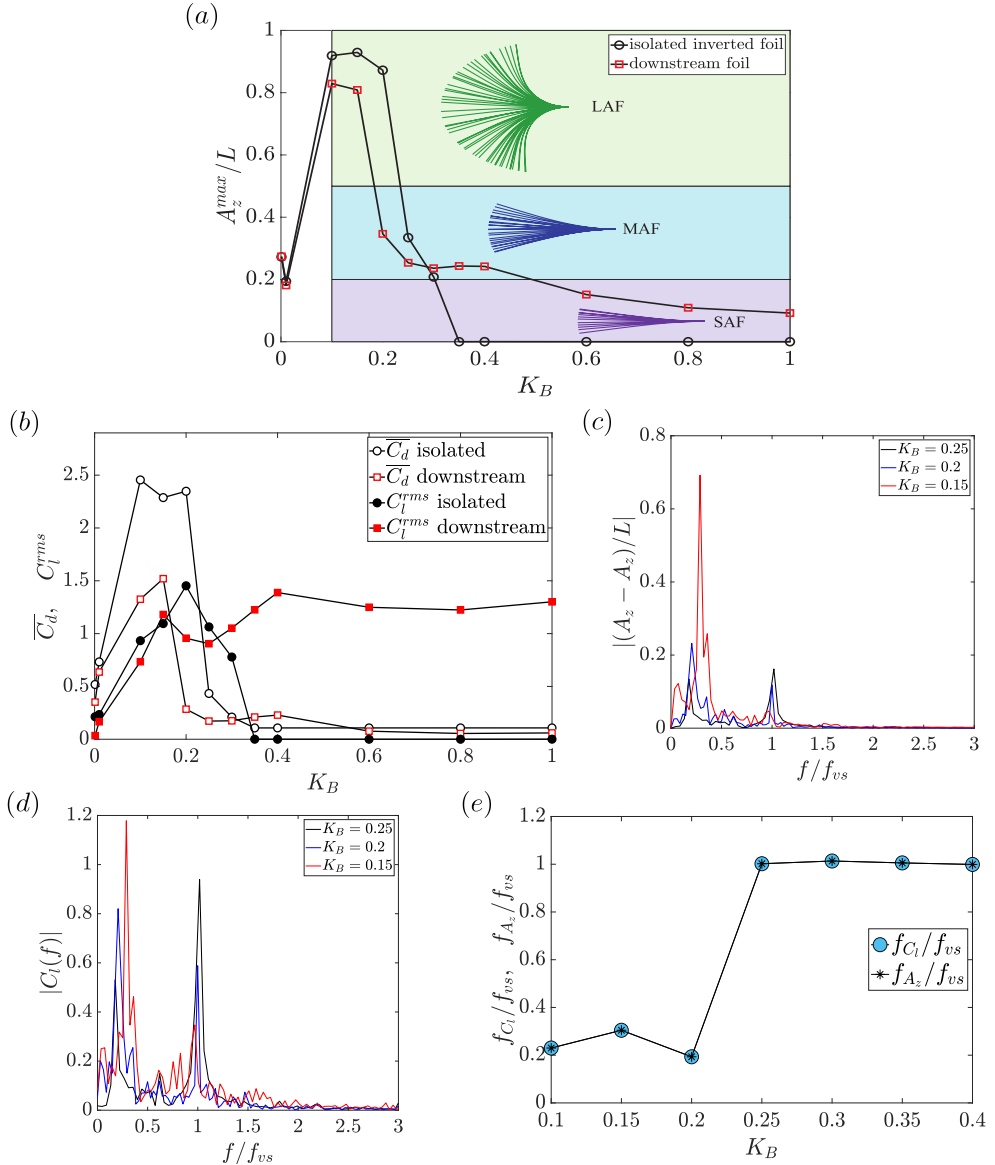


Figure 2: Response characteristics of the inverted foil at  $Re = 1000$  and  $m^* = 0.1$ : (a) variation of maximum transverse tip displacement for the isolated and downstream foil as a function of  $K_B$ , (b) variation of fluid loading the isolated and downstream foil as a function of  $K_B$ , (c-d) power spectra of the transverse vibration amplitudes and lift forces for the downstream foil at  $K_B = [0.15, 0.2, 0.25]$ , (e) variation of flapping and lift frequencies on bending stiffness  $K_B$ .

note that at the considered separation distance  $g^* = 2.8L$ , the downstream inverted foil, does not influence the cylinder dynamics. Therefore, a constant  $f_{vs} = 1.9342$  is observed for all values of  $K_B$  based on the Strouhal number of 0.21. Multiple frequencies exist in both the temporal response of  $C_l$  and  $(A_z - \overline{A}_z)/L$  that are demonstrated by the two dominant peaks observed in the frequency spectra till  $K_B > 0.2$ , below which a single dominant frequency is recorded.

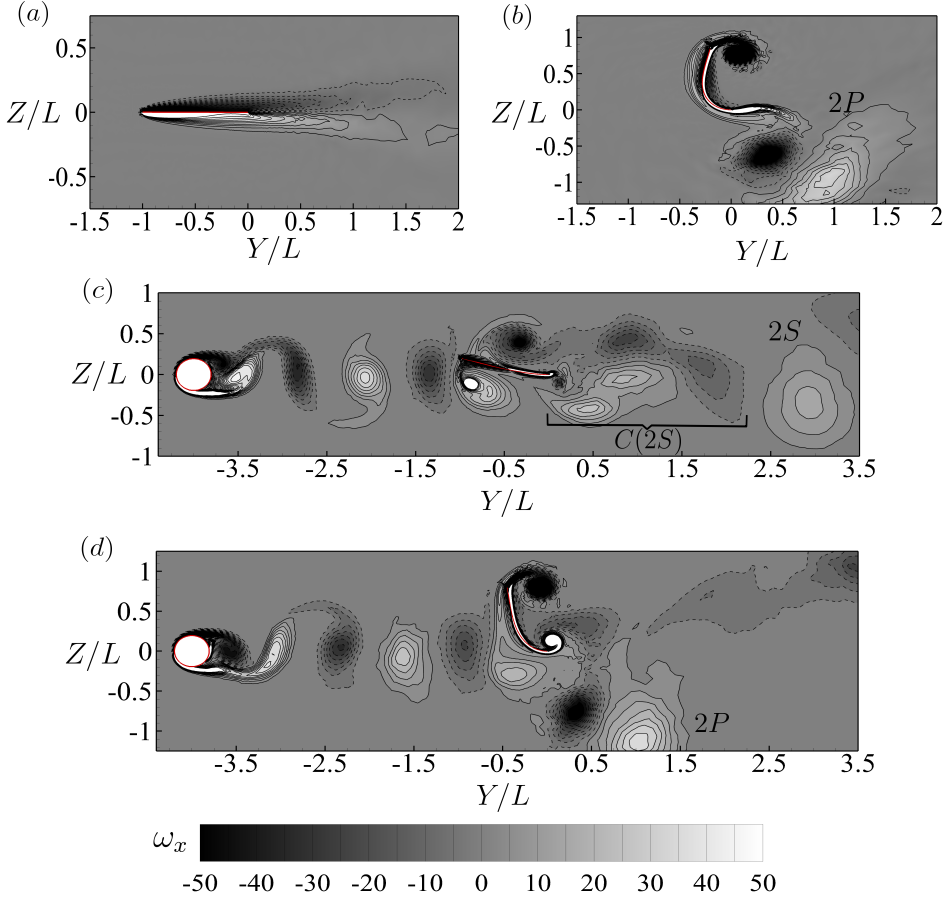


Figure 3:  $x$ -vorticity contours at  $Re = 1000$ ,  $m^* = 0.1$  for: (a-b) isolated foil at  $K_B = 0.35$  and  $K_B = 0.15$ , (c-d) downstream foil at  $K_B = 0.35$ , and  $K_B = 0.15$ . The dotted and solid lines represent negative and positive vorticity contours, respectively.

Figure 2e demonstrates the variation of the dominant frequency ratio of the transverse force  $f_{C_l}/f_{v_s}$  and tip displacement  $f_{A_z}/f_{v_s}$  of the downstream foil with  $K_B$ . A frequency match exists between the transverse tip displacement and lift force for all values of  $K_B$ . We observe that for  $K_B \geq 0.25$ , the dominant frequency  $f_{C_l} \approx f_{A_z} \approx f_{v_s}$  and is unaffected by the change in foil flexibility. A sharp decline in the dominant frequency ratio is observed for  $K_B < 0.25$  with  $f_{A_z} \approx f_{C_l} \approx 0.2f_{v_s}$ . These results demonstrate that for  $K_B > 0.25$ , the cylinder wake strongly influences the inverted foil' response, wherein the foil's motion is synchronized with the cylinder vortex shedding frequency. During synchronization, depending on foil flexibility, the inverted foil undergoes high-frequency oscillations with either small or moderate amplitudes. Below  $K_B = 0.25$ , the influence of the wake reduces, and the foil is no longer synchronized with the cylinder wake. As a result, the downstream foil rapidly starts oscillating in LAF mode, similar to an isolated foil, as  $K_B$  is reduced.

### 3.2. Influence of wake interference on flow field characteristics

We next investigate the vortex organization and formation for the inverted foil for  $K_B \in [0.1, 1]$  in both configurations. Figures 3(a-b) and 3(c-d) represent the vorticity contours for the isolated foil and downstream inverted foil at the maximum tip displacement above

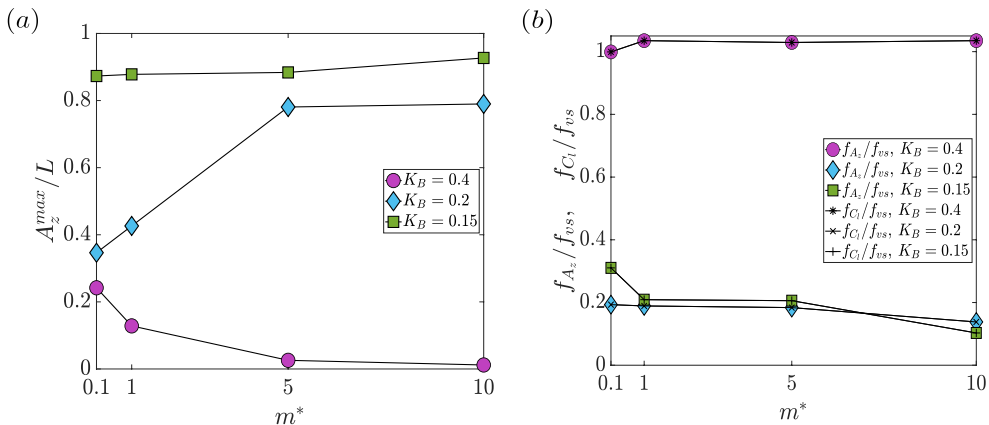


Figure 4: Response characteristics of the downstream foil when  $m^* \in [0.1, 10]$  at  $K_B = [0.15, 0.2, 0.4]$ : (a) variation of maximum transverse tip displacement as a function of  $m^*$ , and (b) variation of oscillation and lift frequency as a function of  $m^*$

$Z/L = 0$  at  $K_B = 0.35$  and  $0.15$ , respectively. As demonstrated in these figures, for the tandem arrangement, a steady Kármán wake is generated in the cylinder wake in the 2S shedding mode as described by (Williamson and Roshko 1988). The wake vortices interfere with the shear layer developed on the downstream foil surface and induce flapping instability for a higher  $K_B$  value at which the isolated foil is still in the stable state, as shown in figures 3a and 3c. Consequently, two single opposite signed vortices are generated on the foil and shed into the wake per one time period, which coalesce with the same signed vortices in the foil's immediate vicinity, resulting in a C(2S) vortex shedding pattern observed in the near wake of foil (Williamson and Roshko 1988). The C(2S) pattern quickly develops into the 2S pattern further downstream. Our investigation revealed a similar wake topology in the tandem arrangement for  $K_B > 0.25$ .

At  $K_B = 0.15$ , the downstream foil oscillates in the LAF regime similar to an isolated foil as demonstrated by figures 3b and 3d. The wake vortices flow above and below the foil surface and interact with the foil's shed vortices in the near wake. As a result, two pairs of vortices are shed over one cycle, resulting in a 2P vortex pattern observed in the wakes like the isolated foil. This 2P pattern is observed for the downstream foil for  $K_B \in [0.1, 0.2]$ . Based on these results, for  $K_B \in [0.1, 1]$  primarily, two vortex-shedding patterns are observed in the wake of the downstream foil. The 2S mode is observed for  $K_B \geq 0.25$ , below which 2P mode is observed. Thus, we can deduce that when the inverted foil is synchronized with the vortex shedding of the upstream cylinder, it undergoes 2S vortex shedding like the cylinder. Below  $K_B = 0.25$ , the foil starts behaving like an isolated foil and no longer oscillates in sync with the cylinder vortex shedding. The consequent change in flapping frequency leads to a change in the vortex shedding pattern from 2S to 2P mode.

### 3.3. Effect of mass ratio $m^*$

We next investigate the influence of mass ratio on the inverted foil's response in the tandem setup. Figures 4a and 4b show the maximum transverse tip amplitude and the oscillation frequency as a function of the mass ratio at  $K_B = 0.15, 0.2$  and  $0.4$ . It is worth noting that the flapping amplitude is synchronized with the lift force acting on the foil for all cases. These figures show three distinct trends observed in the flapping response for varying  $K_B$  and  $m^*$ . At  $K_B = 0.4$ , the flapping amplitude monotonically reduces as  $m^*$  increases. Moreover, synchronization between the foil and the cylinder wake is observed for all values of  $m^*$ . For



moderately flexible foil at  $K_B = 0.2$ , when  $m^*$  is increased, the flapping amplitude steadily grows and saturates at  $A_z^{max}/L \approx 0.78$ . Meanwhile, a marginal decrease is observed in the flapping frequency. At  $K_B = 0.15$ , the flapping amplitude is mostly unaffected by the variation of  $m^*$ . Similar to  $K_B = 0.2$ , an increase in  $m^*$  results in a decrease in the flapping frequency; however, the influence of  $m^*$  is comparatively stronger. As shown in figure 4b, synchronization between the cylinder vortex shedding and the foil is not observed for any value of  $m^*$  at  $K_B = 0.15$  and  $0.2$ .

As presented in §3.1, for  $m^* = 0.1$  and  $K_B = 0.4$ , the inverted foil is relatively stiff, and it undergoes a flapping response induced by the unsteady wake through the synchronization process. Owing to the increase in the foil's inertia force as  $m^*$  increases, the unsteady loading from the wake is insufficient in balancing the inertia forces and maintaining the flapping amplitude. When stiffness is reduced, changes in  $m^*$  have a drastically different effect on the flapping amplitudes, as shown in figure 4a.

At  $m^* = 0.1$  and  $K_B = 0.2$ , the downstream foil, due to decreased stiffness, the foil is no longer synchronized with the wake. However, due to wake interference, the downstream foil undergoes flapping in the MAF regime, as shown in figure 4b. When the mass ratio is increased, the influence of wake flow on the inverted foil dynamics reduces owing to the increase in the density of the foil. As a result, the downstream foil now undergoes flapping in the LAF-like mode observed in an isolated foil counterpart.

At  $K_B = 0.15$ , the inverted foil is highly flexible, and the cylinder wake has limited influence on the downstream foil flapping dynamics. It undergoes LAF with maximum peak-to-peak amplitudes of  $A_z^{max}/L \approx 0.85$  at  $m^* = 0.1$  as observed in figure 4a. The flapping motion is driven predominantly by the combined effect of periodic vortex shedding from the foil and its inherent fluid-elastic instability, akin to an isolated foil (Kim et al. 2013). As a result, when  $m^*$  increases, the dampening effect on the foil's inertia forces by the wake is reduced, leading to a marginal increase in the flapping amplitude and decrease in the frequency. Based on these results, it is evident that in the tandem arrangement of foils with higher stiffness values, the effect of the upstream cylinder is more predominant for lighter foils as compared to heavier foils.

## 4. Conclusion

In this work, we have investigated the response of an inverted foil when placed in tandem with a stationary circular cylinder using high-fidelity numerical simulations. The dynamics are explored systematically as a function of the non-dimensional bending stiffness and mass ratio at a fixed Reynolds number and the gap ratio. Our analysis demonstrates that due to interaction with the cylinder's unsteady wake, the inverted foil experiences a larger transverse fluid loading than the isolated case. Consequently, the downstream becomes unstable for a higher stiffness value and undergoes sustained oscillations for a wider range of the non-dimensional bending stiffness. As a function of increasing flexibility, two additional flapping modes are observed for the downstream foil before it transitions to large amplitude flapping mode: (i) small amplitude flapping and (ii) moderate amplitude flapping modes.

There exists a critical non-dimensional bending stiffness value of  $K_{B,Cr} = 0.25$ , above which synchronization between the downstream foil and cylinder vortex shedding is observed, which drives the foil's flapping response. During synchronization, the inverted foil oscillates with small to moderate amplitudes as stiffness is reduced. Also, a C(2S) shedding pattern wake is observed, which quickly develops to a 2S pattern in the near wake of the foil. Below this threshold stiffness, the cylinder loses control over the foil, and the downstream foil undergoes sustained flapping like an isolated foil. Upon investigating the downstream inverted foil dynamics at different mass ratios, our results indicated that, compared to uniform

flow, when subject to the unsteady wake of a bluff body, the wake interference effects on the foil, along with the occurrence of various flapping modes, are highly influenced by the mass ratio. These results can be applied towards the development of novel optimization and control concepts that maximize the energy-harvesting potential of inverted foils as well as ensure a consistent energy output. Eventually, these control strategies can be leveraged for the design of efficient and robust inverted foil-based energy-harvesting array systems.

**Acknowledgements.** The research was enabled in part through computational resources and services provided by The Digital Research Alliance of Canada (<https://ccdb.alliancecan.ca/>) and the Advanced Research Computing facility at the University of British Columbia (<https://arc.ubc.ca/>).

**Funding.** The authors would like to acknowledge the Natural Sciences and Engineering Research Council of Canada (NSERC) for funding the project.

**Author ORCIDs.** A. Parekh, <https://orcid.org/0009-0007-3454-7871>

**Declaration of Interests.** The authors report no conflict of interest.

## REFERENCES

- SHELLEY, M. J., ZHANG, J. 2011 Flapping and bending bodies interacting with fluid flows, *Ann. Rev. Fluid Mech.*, **43**, pp. 449–465.
- KIM, D., COSSÉ, J., CERDEIRA, C. H., AND GHARIB, M. 2013 Flapping dynamics of an inverted flag, *J. Fluid Mech.*, **736**, pp. R1.
- MICHELIN, S. AND DOARÉ, O. 2013 Energy harvesting efficiency of piezoelectric flags in axial flows, *J. Fluid Mech.*, **714**, pp. 489–504.
- GURUGUBELLI, P. S., AND JAIMAN, R. K. 2008 Self-induced flapping dynamics of a flexible inverted foil in a uniform flow, *J. Fluid Mech.*, **781**, pp. 657–694.
- SADER, J. E., COSSÉ, J., KIM, D., FAN, B., AND GHARIB, M. 2016 Large-amplitude flapping of an inverted flag in a uniform steady flow—a vortex-induced vibration, *J. Fluid Mech.*, **793**, pp. 524–555.
- GURUGUBELLI, P. S., AND JAIMAN, R. K. 2019 Large amplitude flapping of an inverted elastic foil in uniform flow with spanwise periodicity, *J. Fluid and Structures*, **90**, pp. 139–163.
- TANG, C., LIU, N. S., AND LU, X. Y. 2015 Dynamics of an inverted flexible plate in a uniform flow, *Physics of Fluids*, **27**.
- SHOELE, K., AND MITTAL, R. 2016 Energy harvesting by flow-induced flutter in a simple model of an inverted piezoelectric flag *J. Fluid Mech.*, **790**, pp. 582–606.
- ALLEN, J. J., AND A. J. SMITS 2001 Energy Harvesting Eel *J. Fluid and Structures.*, **15**, pp 629-640.
- AKCABAY, D. T., AND YOUNG, Y. L. 1990 Hydroelastic response and energy harvesting potential of flexible piezoelectric beams in viscous flow *Physics of Fluids*, **24**.
- ORREGO, S., SHOELE, K., RUAS, A., DORAN, K., CAGGIANO, B., MITTAL, R. AND KANG, S.H. 2017 Harvesting ambient wind energy with an inverted piezoelectric flag. *Applied Energy*, **194**, pp. 212–222.
- ALAM, M. M., CHAO, L. M., REHMAN, S., JI, C., AND WANG, H. 2021 Energy harvesting from passive oscillation of inverted foil. *Physics of Fluids*, **33**.
- OJO, OLUWAFEMI, EETU KOHTANEN, AOJIA JIANG, JACOB BRODY, ALPER ERTURK, AND KOUROSH SHOELE 2022 Flapping dynamics of an inverted flag behind a cylinder *Bioinspiration and Biomimetics*, **17**, p. 065011.
- KIM, H., KANG, S., AND KIM, D. 2017 Dynamics of a flag behind a bluff body *J. Fluids and Structures*, **71**, pp. 1–154.
- LIU, J., JAIMAN, R. K., AND GURUGUBELLI, P. S. 2014 A stable second-order scheme for fluid–structure interaction with strong added-mass effects. *J. Comp Phys.*, **270**, pp. 687–710.
- ZDRAVKOVICH, MM 1987 The effects of interference between circular cylinders in cross flow *J. Fluid and Structures*, **1**, pp. 239–261.
- SHARMAN, B., LIEN, F. S., DAVIDSON, L., AND NORBERG, C. 2005 Numerical predictions of low Reynolds number flows over two tandem circular cylinders *Int. J. Num. Methods in Fluids*, **45**, pp. 423–447.
- WILLIAMSON, C.H. AND ROSKHO, A. 1988 Vortex formation in the wake of an oscillating cylinder *J. Fluids and Structures*, **7**, pp. 355-381.